Journal of Computational Physics 447 (2021) 110661

Contents lists available at ScienceDirect

Journal of Computational Physics

www.elsevier.com/locate/jcp

A compact and efficient high-order gas-kinetic scheme

Shiyi Li [a], Dongmi Luo [a], Jianxian Qiu [b], Yibing Chen [a,*]

[a] Institute of Applied Physics and Computational Mathematics, Beijing 100191, China
[b] School of Mathematical Sciences and Fujian Provincial Key Laboratory of Mathematical Modeling and High-Performance Scientific Computation, Xiamen University, Xiamen, Fujian 361005, China

ARTICLE INFO

Article history:
Available online 24 August 2021

Keywords:
Compact
WENO
Gas-kinetic scheme
Fifth-order accuracy in both space and time

ABSTRACT

In this paper, a compact fifth-order gas-kinetic scheme (GKS) is proposed to solve the Euler equations of compressible flows. It is based on the framework of a one-stage efficient high-order GKS (EHGKS), which can achieve arbitrary high-order accuracy in both space and time, and the newly-developed compact reconstruction technique, combining both the ideas of the simple weighted essentially non-oscillatory scheme (WENO) and Hermite WENO (HWENO). The evolution model of EHGKS provides the time-dependent variables at cell interfaces, which can directly compute the cell-average slope. Thus the necessary information for a fifth-order compact HWENO reconstruction technique is obtained, and also making it possible to improve simple WENO as a compact reconstruction by determining the quartic polynomial based on the compact stencil. The one-stage time discretization technique of EHGKS makes it possible to utilize the reconstruction only once in each computing time step, which is very different from the present compact multi-stage GKS schemes. The newly-developed compact reconstruction provides the polynomial, not only the pointwise variables but also their spatial derivatives for the interface variables evaluations directly. Several numerical examples are given to validate the accuracy and effectiveness of the proposed compact one-stage scheme. And the numerical results also demonstrate that the new scheme is more efficient than the original EHGKS method with WENO reconstruction technique.

© 2021 Elsevier Inc. All rights reserved.

1. Introduction

In the past decades, the high-order schemes have made great progress and become one of the most important issues in the region of computational fluid dynamics. There are two kinds of schemes to achieve the high-order accuracy in space: one is represented by the essentially non-oscillatory scheme (ENO) and WENO [11,24], which need to expand the stencil of computational cells to provide the necessary information for reconstruction; another one is represented by the discontinuous Galerkin method (DG) [4], the spectral volume scheme (SV) [30], the residual distribution scheme (RD) [1] and HWENO [21,22,20], which can use the compact stencil of computational cells at the cost of solving additional equations. And there are also two approaches to achieve the high-order accuracy in time: the multi-stage methods and the one-stage methods. In generally, the multi-stage methods, which need to evolve several times in each computing time step, are easier to implement [4,24]. On the contrary, the one-stage methods, which evolve only once per step, are often more efficient especially in the case of very high order of accuracy [28,29,27,14]. Based on the above understanding, the one-stage

* Corresponding author.
E-mail addresses: lishiyi14@tsinghua.org.cn (S. Li), dongmiluo@stu.xmu.edu.cn (D. Luo), jxqiu@xmu.edu.cn (J. Qiu), chen_yibing@iapcm.ac.cn (Y. Chen).

https://doi.org/10.1016/j.jcp.2021.110661
0021-9991/© 2021 Elsevier Inc. All rights reserved.

discretization in time and the compact stencil in space should be an optimal choice for high-order schemes. However, this strategy has suffered the following difficulties:

(1) Most of the one-stage methods are based on the Lax-Wendroff procedure [27]. And the complexity of these schemes will increase rapidly with the improvement of the order of accuracy. That is why we can find many one-stage methods are not higher than the fourth order in literature, such as the generalized Riemann problem solver (GRP) [12] and the high-order GKS (HGKS) [13,15,9,16].
(2) The typical compact high-order methods, such as DG and HWENO, often need to solve additional equations to evolve the necessary information for reconstruction [4,21]. It will significantly increase the computation cost [5,7].
(3) The one-stage methods always need to reconstruct all the derivatives of variables at cell interfaces, and the function-based reconstruction is recommended [10,8,17,18]. It is necessary to introduce extra transformation if we use the existing WENO [24,2] and HWENO [21,7,5], since they only provide the reconstruction of pointwise variables.

Recently, great efforts have been made in this issue. The high-order GRP and HGKS, using HWENO instead of WENO for reconstruction, have been extended to the compact high-order schemes [5,7,10]. However, these methods are all multi-stage in time. To our knowledge, there is no one-stage and compact high-order method which can overcome all the above three difficulties at the same time. And the new scheme in this literature will give a solution.

The recently-developed EHGKS scheme not only preserves the advantages of the original HGKS, which can achieve high-order accuracy and robustness, but also significantly reduces the complexity and computation cost of the original HGKS [14]. It ensures EHGKS can be extended to arbitrary high-order accuracy [14]. Although the current EHGKS scheme used the traditional pointwise WENO reconstruction method, which didn't solve the difficulties (2) and (3), it provides a general framework to design a one-stage and compact high-order scheme.

The original EHGKS scheme is an efficient and easy-implement one-stage high-order method. Its evolution model can provide the time evolution of the variables at cell interfaces. This information enables to design a function-based compact reconstruction technique, which combines the ideas of simple WENO [35,36] and HWENO [21,10]. The combination of EHGKS and the newly-developed reconstruction technique builds an efficient and compact fifth-order one-stage method, and it can overcome all the above three difficulties.

This paper is organized as follows. In Section 2.1, the original EHGKS scheme is briefly reviewed. In Section 2.2, the compact EHGKS is obtained by simply introducing the existing HWENO reconstruction method. In Section 2.3, the new compact and function-based reconstruction technique is introduced. In Section 3, we extend the new scheme to the two-dimensional case. In Section 4, numerous numerical tests are present to demonstrate the good performance of our new scheme. The conclusions are made in the last section.

2. The compact and efficient fifth-order gas-kinetic scheme: the one-dimensional case

EHGKS [14] is reviewed firstly in this section. Then the compact scheme which simply uses the existing HWENO technique in the framework of EHGKS is proposed in Section 2.2. In Section 2.3, a new compact and function-based reconstruction technique and the corresponding scheme are developed.

2.1. The framework of EHGKS

EHGKS is devoted to solving the Euler equations of compressible flows [14]:

$$\frac{\partial \mathbf{W}}{\partial t} + \frac{\partial \mathbf{F}}{\partial x} = \mathbf{0}, \tag{1}$$

where the conservative variable $\mathbf{W} = (\rho, \rho U, \rho E)^{\mathrm{T}}$ and the Euler flux $\mathbf{F} = (\rho U, \rho U^2 + p, \rho E U + pU)^{\mathrm{T}}$. ρ is the density. U is the velocity. The total energy $\rho E = \frac{1}{2}\rho U^2 + p/(\gamma - 1)$, where p is the pressure and γ is the specific heat ratio.

Under the finite volume framework, the space domain is divided into N uniform cells $I_i = [x_{i-\frac{1}{2}}, x_{i+\frac{1}{2}}]$, $i = 1, 2, \cdots, N$. The cell is indexed as i. The cell size $\Delta x = x_{i+\frac{1}{2}} - x_{i-\frac{1}{2}}$. The time is discretized as $t^0, t^1, \cdots, t^n, \cdots$. Denote the time step by $\Delta t = t^{n+1} - t^n$. Let $\overline{\mathbf{W}}_i^n$ be the cell-average variable of $\mathbf{W}(x, t)$ in the i-th cell at time t^n. Under the fully discrete framework, $\overline{\mathbf{W}}_i^{n+1}$ is updated by

$$\overline{\mathbf{W}}_i^{n+1} = \overline{\mathbf{W}}_i^n - \frac{1}{\Delta x}\left(\mathscr{J}_{i+\frac{1}{2}} - \mathscr{J}_{i-\frac{1}{2}}\right), \tag{2}$$

where

$$\mathscr{J}_{i+\frac{1}{2}} = \int_{t^n}^{t^{n+1}} \mathbf{F}(x_{i+\frac{1}{2}}, t)\mathrm{d}t \tag{3}$$

is the time integrated flux at the cell boundary $x = x_{i+\frac{1}{2}}$. EHGKS provides an efficient and robust solver for the flux evaluation $\mathbf{F}(x_{i+\frac{1}{2}}, t)$ and its time integral with arbitrary high-order accuracy [14]. The construction procedure is illustrated as follows.

EHGKS is based on the BGK equation [14]:

$$\frac{\partial f}{\partial t} + u\frac{\partial f}{\partial x} = \frac{g - f}{\tau}, \tag{4}$$

where the particle distribution function $f = f(x, t, u, \xi)$ [23]. u is the particle velocity and ξ is the internal variable [23]. The mean collision time $\tau = \mu/p$, where μ is the dynamical viscosity [23]. g is the Maxwellian equilibrium state [23]

$$g = \rho\left(\frac{\lambda}{\pi}\right)^{\frac{K+1}{2}} \mathrm{e}^{-\lambda\left((u-U)^2+\xi^2\right)}. \tag{5}$$

g can be determined by $g = g(\mathbf{W})$. $\lambda = 1/(2RT)$, where T is the temperature and R is the gas constant. The degree of freedom $K = (3-\gamma)/(\gamma-1)$ [32]. The time integral solution of the BGK equation is given by [32]

$$f(x, t, u, \xi) = \frac{1}{\tau}\int_0^t g(x', t', u, \xi)\mathrm{e}^{-(t-t')/\tau}\mathrm{d}t' + \mathrm{e}^{-t/\tau} f(x - ut, 0, u, \xi), \tag{6}$$

where $x' = x - u(t - t')$. Here we take $t^n = 0$ for simplicity. After taking the moments, the relationships between f and $\mathbf{W}$, f and $\mathbf{F}$ are

$$\mathbf{W}(x, t) = \int f(x, t, u, \xi)\mathbf{\Psi}\mathrm{d}\Xi, \tag{7}$$

$$\mathbf{F}(x, t) = \int u f(x, t, u, \xi)\mathbf{\Psi}\mathrm{d}\Xi, \tag{8}$$

where the moment vector $\mathbf{\Psi} = (1, u, (u^2 + \xi^2)/2)^{\mathrm{T}}$ and $\mathrm{d}\Xi = \mathrm{d}u\mathrm{d}\xi$. Details on the moments can be referred in [32,14].

According to the derivations in [14], the simplified evolution model to construct the $(r+1)$-th-order EHGKS is

$$f(x_{i+\frac{1}{2}}, t, u, \xi) = \left(1 - \mathrm{e}^{-\Delta t/\tau}\right)\sum_{l=0}^{r}\frac{t^l}{l!}\frac{\partial^l g^e}{\partial t^l} + \mathrm{e}^{-\Delta t/\tau}\sum_{l=0}^{1}\frac{(-ut)^l}{l!}\frac{\partial^l g^0}{\partial x^l}. \tag{9}$$

Here we take $x_{i+\frac{1}{2}} = 0$ for simplicity. g^0 is the pointwise distribution function:

$$g^0 = \begin{cases} g(\mathbf{W}^{\mathrm{L}}_{i+\frac{1}{2}}), & u \geq 0, \\ g(\mathbf{W}^{\mathrm{R}}_{i+\frac{1}{2}}), & u < 0. \end{cases} \tag{10}$$

The pointwise values $\mathbf{W}^{\mathrm{L}}_{i+\frac{1}{2}} = \lim_{x\to x_{i+\frac{1}{2}}} \mathbf{W}^n_i(x)$ and $\mathbf{W}^{\mathrm{R}}_{i+\frac{1}{2}} = \lim_{x\to x_{i+\frac{1}{2}}} \mathbf{W}^n_{i+1}(x)$. $\mathbf{W}^n_i(x)$ is the polynomial over the i-th cell. $g^e = g(\mathbf{W}^e_{i+\frac{1}{2}})$ where $\mathbf{W}^e_{i+\frac{1}{2}}$ is determined by the conservation constraint [32]:

$$\mathbf{W}^e_{i+\frac{1}{2}} = \int g^0\mathbf{\Psi}\mathrm{d}\Xi. \tag{11}$$

The spatial and temporal derivatives of g^0 and g^e can be derived from the corresponding derivatives of $\mathbf{W}^{\mathrm{L,R}}_{i+\frac{1}{2}}$ and $\mathbf{W}^e_{i+\frac{1}{2}}$ [32]. The spatial derivatives of $\mathbf{W}^e_{i+\frac{1}{2}}$ are weighted from those of $\mathbf{W}^{\mathrm{L,R}}_{i+\frac{1}{2}}$:

$$\frac{\partial^m \mathbf{W}^e_{i+\frac{1}{2}}}{\partial x^m} = \omega^e\frac{\partial^m \mathbf{W}^{\mathrm{L}}_{i+\frac{1}{2}}}{\partial x^m} + \left(1 - \omega^e\right)\frac{\partial^m \mathbf{W}^{\mathrm{R}}_{i+\frac{1}{2}}}{\partial x^m}, \quad 1 \leq m \leq r, \tag{12}$$

where $\omega^e = erfc(-\sqrt{\lambda^e_{i+\frac{1}{2}}}U^e_{i+\frac{1}{2}})/2$ and $erfc$ is the complementary error function [14]. The temporal derivatives are obtained after the Lax-Wendroff transformations and the details can be referred in [14]. In EHGKS, τ is given by

$$\tau = \epsilon_1\Delta t + \epsilon_2\frac{\left|p^{\mathrm{L}}_{i+\frac{1}{2}} - p^{\mathrm{R}}_{i+\frac{1}{2}}\right|}{p^{\mathrm{L}}_{i+\frac{1}{2}} + p^{\mathrm{R}}_{i+\frac{1}{2}}}\Delta t, \tag{13}$$

where ϵ_1 and ϵ_2 are the constant parameters [14].

Given by Eqs. (8), (9) and (3), the time integrated flux of EHGKS at the cell boundary $x_{i+\frac{1}{2}}$ is evaluated by [14]

$$\mathscr{J}_{i+\frac{1}{2}} = \left(1 - \mathrm{e}^{-\Delta t/\tau}\right) \mathbb{F}^{e}_{i+\frac{1}{2}}(\Delta t) + \mathrm{e}^{-\Delta t/\tau} \mathbb{F}^{k}_{i+\frac{1}{2}}(\Delta t), \tag{14}$$

where

$$\mathbb{F}^{e}_{i+\frac{1}{2}}(\Delta t) = \sum_{l=0}^{r} \iint_{t^n}^{t^{n+1}} \frac{t^l}{l!} \frac{\partial^l u g^e}{\partial t^l} \mathbf{\Psi} \mathrm{d}\Xi \mathrm{d}t,$$

$$\mathbb{F}^{k}_{i+\frac{1}{2}}(\Delta t) = \sum_{l=0}^{1} \iint_{t^n}^{t^{n+1}} \frac{(-ut)^l}{l!} \frac{\partial^l u g^0}{\partial x^l} \mathbf{\Psi} \mathrm{d}\Xi \mathrm{d}t.$$

For higher efficiency, $\mathbb{F}^{e}_{i+\frac{1}{2}}(\Delta t)$ is evaluated by a similar way to the state expansion of the ADER method [25], which introduced the Gaussian rule based on the concept of the generalized Riemann problem to integrate the flux [25]. EHGKS uses the same Gaussian rule [25,26] based on $\mathbf{Q}^e = (\rho^e, U^e, p^e)^{\mathrm{T}}$ to approximate $\mathbb{F}^{e}_{i+\frac{1}{2}}(\Delta t)$ [14]:

$$\mathbb{F}^{e}_{i+\frac{1}{2}}(\Delta t) \approx \sum_{\alpha=0}^{\hat{K}} \mathcal{F}_{Eu}\left(\mathcal{Q}^e\left(\kappa_\alpha \Delta t\right)\right) \omega_\alpha, \tag{15}$$

where

$$\mathcal{Q}^e(t) = \sum_{l=0}^{r} \frac{t^l}{l!} \frac{\partial^l \mathbf{Q}^e_{i+\frac{1}{2}}}{\partial t^l}. \tag{16}$$

Here $\mathcal{F}_{Eu}(\mathbf{Q}) = (\rho U, \rho U^2 + p, \rho E U + p U)^{\mathrm{T}}$. $\hat{K} + 1$ is the number of the Gaussian nodes. κ_α is the scaled node. ω_α is its weight. The fifth-order EHGKS takes $r = 4$, $\hat{K} = 2$, $(\kappa_0, \kappa_1, \kappa_2) = (1/2 - \sqrt{15}/10, 1/2, 1/2 + \sqrt{15}/10)$ and $(\omega_0, \omega_1, \omega_2) = (5/18, 4/9, 5/18)$ [14]. Based on the Lax-Wendroff procedure, the temporal derivatives of $\mathbf{Q}^e_{i+\frac{1}{2}}$ are transformed from the spatial derivatives of $\mathbf{Q}^e_{i+\frac{1}{2}}$, which can be calculated by the spatial derivatives of $\mathbf{W}^e_{i+\frac{1}{2}}$ [14]. $\mathbb{F}^{k}_{i+\frac{1}{2}}(\Delta t)$ is the second-order KFVS flux to provide robustness [14].

The current EHGKS scheme in [14] used the traditional WENO technique for reconstruction. To obtain the necessary information $\mathbf{W}^{\mathrm{L,R}}_{i+\frac{1}{2}}$ and $\frac{\partial^m \mathbf{W}^{\mathrm{L,R}}_{i+\frac{1}{2}}}{\partial x^m}$ for flux evaluation, the reconstruction procedure is [14]:

Step (1). Based on the stencil $\{I_{i-2}, I_{i-1}, I_i, I_{i+1}, I_{i+2}\}$, utilize the traditional characteristic WENO reconstruction to obtain the pointwise values $\mathbf{W}^{\mathrm{L}}_{i+\frac{1}{2}}$ and $\mathbf{W}^{\mathrm{R}}_{i-\frac{1}{2}}$.

Step (2). Based on the two pointwise values $\{\mathbf{W}^{\mathrm{L}}_{i+\frac{1}{2}}, \mathbf{W}^{\mathrm{R}}_{i-\frac{1}{2}}\}$ and the centremost cell averages $\{\overline{\mathbf{W}}^n_{i-1}, \overline{\mathbf{W}}^n_i, \overline{\mathbf{W}}^n_{i+1}\}$, implement the linear reconstruction to approximate the polynomial $\mathbf{W}^n_i(x)$ over the cell, and then calculate the spatial derivatives $\frac{\partial^m \mathbf{W}^{\mathrm{L}}_{i+\frac{1}{2}}}{\partial x^m}$ and $\frac{\partial^m \mathbf{W}^{\mathrm{R}}_{i-\frac{1}{2}}}{\partial x^m}$.

The current EHGKS scheme is denoted by EHGKS-WENO in this paper. EHGKS-WENO is not compact and has room to improve its efficiency in reconstruction.

2.2. Utilization of HWENO in the framework of EHGKS

Following the ideas of the compact multi-stage methods [5,7], the i-th cell-average slope, which is defined as

$$\overline{\mathbf{W}'}^n_i = \frac{1}{\Delta x} \int_{x_{i-\frac{1}{2}}}^{x_{i+\frac{1}{2}}} \frac{\partial \mathbf{W}(x, t^n)}{\partial x} \mathrm{d}x,$$

can be directly computed by

$$\overline{\mathbf{W}'}^n_i = \frac{\mathbf{W}(x_{i+\frac{1}{2}}, t^n) - \mathbf{W}(x_{i-\frac{1}{2}}, t^n)}{\Delta x}. \tag{17}$$

According to Eqs. (7) and (9), the fifth-order evolution model of $\mathbf{W}(x_{i+\frac{1}{2}}, t)$ can be evaluated by

$$\mathbf{W}(x_{i+\frac{1}{2}}, t) = \left(1 - \mathrm{e}^{-\Delta t/\tau}\right) \mathbb{W}^{e}_{i+\frac{1}{2}}(t) + \mathrm{e}^{-\Delta t/\tau}\, \mathbb{W}^{k}_{i+\frac{1}{2}}(t), \tag{18}$$

where

$$\mathbb{W}^{e}_{i+\frac{1}{2}}(t) = \sum_{l=0}^{4} \int \frac{t^l}{l!} \frac{\partial^l g^e}{\partial t^l} \mathbf{\Psi} \mathrm{d}\Xi,$$

$$\mathbb{W}^{k}_{i+\frac{1}{2}}(t) = \sum_{l=0}^{1} \int \frac{(-ut)^l}{l!} \frac{\partial^l g^0}{\partial x^l} \mathbf{\Psi} \mathrm{d}\Xi.$$

The high-order term $\mathbb{W}^{e}_{i+\frac{1}{2}}(t)$ can be approximated by

$$\mathbb{W}^{e}_{i+\frac{1}{2}}(t) \approx \mathcal{W}\left(\mathcal{Q}^e(t)\right). \tag{19}$$

Here $\mathcal{W}(\mathbf{Q}) = (\rho, \rho U, \rho E)^{\mathrm{T}}$. $\mathcal{Q}^e(t)$ is obtained by Eq. (16).

On the compact stencil $\{I_{i-1}, I_i, I_{i+1}\}$, the traditional characteristic HWENO reconstruction is straightforward from the information $\{\overline{\mathbf{W}}^n_{i-1}, \overline{\mathbf{W}'}^n_{i-1}, \overline{\mathbf{W}}^n_i, \overline{\mathbf{W}}^n_{i+1}, \overline{\mathbf{W}'}^n_{i+1}\}$ [21]. The details of HWENO can be referred in [21,5,7]. By introducing the HWENO technique in the framework of EHGKS, it's available to construct a one-stage compact scheme with consistent fifth order of accuracy in space and time. It is denoted by EHGKS-HWENO in this paper. However, HWENO can't reconstruct the polynomial $\mathbf{W}^n_i(x)$ directly. The Step (2) in the reconstruction procedure of EHGKS-WENO is still required in EHGKS-HWENO.

2.3. A new compact and function-based reconstruction technique

Inspired by the function-based reconstruction techniques [35,10,17], a new compact and function-based reconstruction technique is introduced in this section. The new reconstruction technique will replace HWENO in EHGKS-HWENO, and construct a new compact one-stage scheme with consistent fifth order of accuracy in both space and time, under the framework of EHGKS.

Based on the information on the compact stencil $\{I_{i-1}, I_i, I_{i+1}\}$, the reconstruction procedure of the new scheme is given as follows. The reconstruction is implemented after transforming to the local characteristic fields [24]. For convenience, the superscript n is abbreviated.

Firstly, define a quartic polynomial $p_1(x) \in span\left\{1, x, x^2, x^3, x^4\right\}$ by requiring

$$\frac{1}{\Delta x} \int_{I_l} p_1(x)\, \mathrm{d}x = \overline{\mathbf{W}}_l, \quad l = i-1, i, i+1,$$

$$\frac{1}{\Delta x} \int_{I_l} \frac{\mathrm{d}p_1(x)}{\mathrm{d}x} \mathrm{d}x = \overline{\mathbf{W}'}_l, \quad l = i-1, i+1.$$

Then define two linear polynomials $p_2(x) \in span\{1, x\}$ and $p_3(x) \in span\{1, x\}$ by requiring

$$\frac{1}{\Delta x} \int_{I_l} p_2(x)\, \mathrm{d}x = \overline{\mathbf{W}}_l, \quad l = i-1, i,$$

$$\frac{1}{\Delta x} \int_{I_l} p_3(x)\, \mathrm{d}x = \overline{\mathbf{W}}_l, \quad l = i, i+1.$$

Inspired by the current function-based reconstruction techniques [35,10,17], $p_1(x)$ can be rewritten as

$$p_1(x) = \gamma_1 \left(\frac{1}{\gamma_1} p_1(x) - \frac{\gamma_2}{\gamma_1} p_2(x) - \frac{\gamma_3}{\gamma_1} p_3(x) \right) + \gamma_2 p_2(x) + \gamma_3 p_3(x),$$

where $\gamma_1, \gamma_2, \gamma_3$ are positive linear weights and $\gamma_1 + \gamma_2 + \gamma_3 = 1$. After introducing the nonlinear weights, the final polynomial over the i-th cell is given by

$$p(x) = \omega_1 \left(\frac{1}{\gamma_1} p_1(x) - \frac{\gamma_2}{\gamma_1} p_2(x) - \frac{\gamma_3}{\gamma_1} p_3(x) \right) + \omega_2 p_2(x) + \omega_3 p_3(x). \tag{20}$$

The nonlinear weights:

$$\omega_l = \frac{\overline{\omega}_l}{\sum_{ll=1}^{3} \overline{\omega}_{ll}}, \overline{\omega}_l = \gamma_l \left(1 + \frac{\tau_0}{\beta_l + \varepsilon}\right), \quad l = 1, 2, 3,$$

where $\tau_0 = (|\beta_1 - \beta_2| + |\beta_1 - \beta_3|)^2/4$ and $\varepsilon = 10^{-6}$. The smoothness indicators are defined as [35]

$$\beta_l = \sum_{k=1}^{\hat{r}} \int_{I_i} \Delta x^{2k-1} \left(\frac{\mathrm{d}^k p_l(x)}{\mathrm{d}x^k}\right)^2 \mathrm{d}x,$$

where $\hat{r} = 4$ for $l = 1$, $\hat{r} = 1$ for $l = 2$ and 3. After some algebraic derivations, the explicit expressions of β_l are

$$\begin{aligned}
\beta_1 = &\frac{781}{320}\left(\overline{\mathbf{W}}_{i-1} - \overline{\mathbf{W}}_{i+1} + \Delta x \overline{\mathbf{W}'}_{i-1} + \Delta x \overline{\mathbf{W}'}_{i+1}\right)^2 \\
&+ \frac{1}{16}\left(3\overline{\mathbf{W}}_{i-1} - 3\overline{\mathbf{W}}_{i+1} + \Delta x \overline{\mathbf{W}'}_{i-1} + \Delta x \overline{\mathbf{W}'}_{i+1}\right)^2 \\
&+ \frac{1421461}{36400}\left(2\overline{\mathbf{W}}_{i-1} - 4\overline{\mathbf{W}}_{i} + 2\overline{\mathbf{W}}_{i+1} + \Delta x \overline{\mathbf{W}'}_{i-1} - \Delta x \overline{\mathbf{W}'}_{i+1}\right)^2 \\
&+ \frac{1}{3900}\left(131\overline{\mathbf{W}}_{i-1} - 262\overline{\mathbf{W}}_{i} + 131\overline{\mathbf{W}}_{i+1} + 33\Delta x \overline{\mathbf{W}'}_{i-1} - 33\Delta x \overline{\mathbf{W}'}_{i+1}\right)^2, \\
\beta_2 = &\left(\overline{\mathbf{W}}_{i-1} - \overline{\mathbf{W}}_{i}\right)^2, \\
\beta_3 = &\left(\overline{\mathbf{W}}_{i} - \overline{\mathbf{W}}_{i+1}\right)^2.
\end{aligned}$$

We can prove the fifth-order accuracy of $p(x)$ to approximate $\mathbf{W}_i^n(x)$. For convenience, denote $\mathbf{W}_i' = \frac{\partial \mathbf{W}_i^n(x_i)}{\partial x}, \mathbf{W}_i'' = \frac{\partial^2 \mathbf{W}_i^n(x_i)}{\partial x^2}, \mathbf{W}_i''' = \frac{\partial^3 \mathbf{W}_i^n(x_i)}{\partial x^3}, \mathbf{W}_i'''' = \frac{\partial^4 \mathbf{W}_i^n(x_i)}{\partial x^4}$. The Taylor expansions of β_l are

$$\begin{aligned}
\beta_1 = &\Delta x^2 \left(\mathbf{W}_i'\right)^2 + \Delta x^4 \left(\frac{1}{12}\left(\mathbf{W}_i'\mathbf{W}_i'''\right) + \frac{13}{12}\left(\mathbf{W}_i''\right)^2\right) \\
&+ \Delta x^6 \left(\frac{1043}{960}\left(\mathbf{W}_i'''\right)^2 - \frac{1}{64}\left(\mathbf{W}_i'\mathbf{W}_i''''\right) + \frac{7}{80}\left(\mathbf{W}_i''\mathbf{W}_i''''\right)\right) + O\left(\Delta x^8\right), \\
\beta_2 = &\Delta x^2 \left(\mathbf{W}_i'\right)^2 - \Delta x^3 \left(\mathbf{W}_i'\mathbf{W}_i''\right) + \Delta x^4 \left(\frac{1}{4}\left(\mathbf{W}_i''\right)^2 + \frac{5}{12}\left(\mathbf{W}_i'\mathbf{W}_i'''\right)\right) + O\left(\Delta x^5\right), \\
\beta_3 = &\Delta x^2 \left(\mathbf{W}_i'\right)^2 + \Delta x^3 \left(\mathbf{W}_i'\mathbf{W}_i''\right) + \Delta x^4 \left(\frac{1}{4}\left(\mathbf{W}_i''\right)^2 + \frac{5}{12}\left(\mathbf{W}_i'\mathbf{W}_i'''\right)\right) + O\left(\Delta x^5\right),
\end{aligned}$$

which give

$$\begin{aligned}
\beta_1 - \beta_2 &= \Delta x^3 \left(\mathbf{W}_i'\mathbf{W}_i''\right) + O\left(\Delta x^4\right), \\
\beta_1 - \beta_3 &= -\Delta x^3 \left(\mathbf{W}_i'\mathbf{W}_i''\right) + O\left(\Delta x^4\right).
\end{aligned}$$

It illustrates $\tau_0 = O\left(\Delta x^6\right)$ and $\tau_0/(\beta_l + \epsilon) = O\left(\Delta x^4\right)$. Consequently $\omega_l = \gamma_l(1 + O(\Delta x^4))$, which guarantees the fifth-order accuracy of $p(x)$ to approximate $\mathbf{W}_i^n(x)$.

Since the new reconstruction technique combines the spirits of simple WENO [35,10] and HWENO [21], it is marked as SHWENO in this paper. Utilization of SHWENO in the framework of EHGKS builds the compact one-stage scheme EHGKS-SHWENO. The cell-average slope $\overline{\mathbf{W}'}_l$ in determining the quartic polynomial $p_1(x)$ is directly computed by Eqs. (17) and (18).

Remark 1. Compared with the current function-based WENO reconstruction technique [35,17], SHWENO introduces the cell-average slope to determine the quartic polynomial, making it possible to reconstruct on a compact stencil. SHWENO can reconstruct the polynomial directly, instead of introducing other transformations in the pointwise WENO methods [21,7,5]. Under the framework of EHGKS, EHGKS-SHWENO directly computes the cell-average slope based on its evolution model, other than solving additional equations for the slope. The new scheme is built under the one-stage framework, which is very different from the compact multi-stage HGKS schemes [9,7,10].

3. The compact and efficient fifth-order gas-kinetic scheme: the two-dimensional case

In this section, EHGKS-SHWENO is extended to the two-dimensional case dimension-by-dimension.

3.1. The framework of EHGKS

In the two-dimensional case, we assume the computational domain is uniformly divided into rectangular cells. The cell indexed as i in the x direction and j in the y direction is indicated as $I_{i,j}$. Its cell area is $\Delta x \times \Delta y$. Let $\overline{\mathbf{W}}^n_{i,j}$ be the cell-average variable of $\mathbf{W}(x,y,t)$ in the cell $I_{i,j}$ and at time t^n. Under the fully discrete finite volume framework, $\overline{\mathbf{W}}^{n+1}_{i,j}$ is updated by

$$\overline{\mathbf{W}}^{n+1}_{i,j} = \overline{\mathbf{W}}^n_{i,j} - \frac{1}{\Delta x}\left(\mathscr{F}_{i+\frac{1}{2},j} - \mathscr{F}_{i-\frac{1}{2},j}\right) - \frac{1}{\Delta y}\left(\mathscr{G}_{i,j+\frac{1}{2}} - \mathscr{G}_{i,j-\frac{1}{2}}\right), \tag{21}$$

where the time integrated flux along the cell interface $(x_{i+\frac{1}{2}}, y_{j-\frac{1}{2}}) \to (x_{i+\frac{1}{2}}, y_{j+\frac{1}{2}})$ is

$$\begin{aligned}
\mathscr{F}_{i+\frac{1}{2},j} &= \int_{y_{j-\frac{1}{2}}}^{y_{j+\frac{1}{2}}} \int_{t^n}^{t^{n+1}} \mathbf{F}(x_{i+\frac{1}{2}}, y, t)\mathrm{d}y\mathrm{d}t, \\
\mathscr{G}_{i,j+\frac{1}{2}} &= \int_{x_{i-\frac{1}{2}}}^{x_{i+\frac{1}{2}}} \int_{t^n}^{t^{n+1}} \mathbf{G}(x, y_{j+\frac{1}{2}}, t)\mathrm{d}x\mathrm{d}t.
\end{aligned} \tag{22}$$

The evolution model of EHGKS at the cell interface is [14]

$$\begin{aligned}
f(x_{i+\frac{1}{2}}, y, t, \mathbf{u}, \boldsymbol{\xi}) = &\left(1 - \mathrm{e}^{-\Delta t/\tau}\right) \sum_{l=0}^{r} \frac{1}{l!}\left(t\frac{\partial}{\partial t} + y\frac{\partial}{\partial y}\right)^l g^e \\
&+ \mathrm{e}^{-\Delta t/\tau} \sum_{l=0}^{1} \frac{(-1)^l}{l!}\left(ut\frac{\partial}{\partial x} + (vt - y)\frac{\partial}{\partial y}\right)^l g^0.
\end{aligned} \tag{23}$$

Here we take $x_{i+\frac{1}{2}} = 0$ and $y_j = 0$ for simplicity. The reconstruction is carried out for the Gaussian nodes along the cell interface. The Gaussian nodes are $(y_{j_0}, y_{j_1}, y_{j_2}) = (-\sqrt{15}/10, 0, \sqrt{15}/10)\Delta y$ [26,14]. g^0 is determined by $\mathbf{W}^{\mathrm{L,R}}_{i+\frac{1}{2},j_1}$, where the pointwise values $\mathbf{W}^{\mathrm{L}}_{i+\frac{1}{2},j_1} = \lim_{x\to x_{i+\frac{1}{2}}} \mathbf{W}^n_{i,j}(x, y_{j_1})$ and $\mathbf{W}^{\mathrm{R}}_{i+\frac{1}{2}} = \lim_{x\to x_{i+\frac{1}{2}}} \mathbf{W}^n_{i+1,j}(x, y_{j_1})$. $g^e = g(\mathbf{W}^e_{i+\frac{1}{2},j_1})$ and $\mathbf{W}^e_{i+\frac{1}{2},j_1}$ is determined by $\mathbf{W}^{\mathrm{L,R}}_{i+\frac{1}{2},j_1}$ according to the conservation constraint [32]. The time integrated flux of EHGKS along the cell interface is evaluated by [14]

$$\mathscr{F}_{i+\frac{1}{2},j} = \left(1 - \mathrm{e}^{-\Delta t/\tau}\right)\mathbb{F}^e_{i+\frac{1}{2},j}(\Delta t) + \mathrm{e}^{-\Delta t/\tau}\mathbb{F}^k_{i+\frac{1}{2},j}(\Delta t), \tag{24}$$

where

$$\begin{aligned}
\mathbb{F}^e_{i+\frac{1}{2},j}(\Delta t) &= \sum_{l=0}^{r} \int_{y_{j-\frac{1}{2}}}^{y_{j+\frac{1}{2}}} \int_{t^n}^{t^{n+1}} \int \frac{1}{l!}\left(t\frac{\partial}{\partial t} + y\frac{\partial}{\partial y}\right)^l u g^e \boldsymbol{\Psi}\mathrm{d}\Xi\mathrm{d}y\mathrm{d}t, \\
\mathbb{F}^k_{i+\frac{1}{2},j}(\Delta t) &= \sum_{l=0}^{1} \int_{y_{j-\frac{1}{2}}}^{y_{j+\frac{1}{2}}} \int_{t^n}^{t^{n+1}} \int \frac{(-1)^l}{l!}\left(ut\frac{\partial}{\partial x} + (vt - y)\frac{\partial}{\partial y}\right)^l u g^0 \boldsymbol{\Psi}\mathrm{d}\Xi\mathrm{d}y\mathrm{d}t.
\end{aligned}$$

$\mathbb{F}^e_{i+\frac{1}{2},j}(\Delta t)$ is approximated by the Gaussian rule [14,26]

$$\mathbb{F}^e_{i+\frac{1}{2},j}(\Delta t) \approx \sum_{\alpha=0}^{\hat{K}} \sum_{\beta=0}^{\hat{K}} \mathcal{F}_{Eu}\left(\mathcal{Q}^e\left(y_{j_\alpha}, \kappa_\beta \Delta t\right)\right)\omega_\alpha\omega_\beta, \tag{25}$$

where $\mathcal{F}_{Eu}(\mathbf{Q}) = (\rho U, \rho U^2 + p, \rho UV, \rho EU + pU)^{\mathrm{T}}$, $\mathbf{Q} = (\rho, U, V, p)^{\mathrm{T}}$ and

$$\mathcal{Q}^e(y,t) = \sum_{l=0}^{r} \frac{1}{l!}\left(t\frac{\partial}{\partial t} + y\frac{\partial}{\partial y}\right)^l \mathbf{Q}^e_{i+\frac{1}{2},j_1}. \tag{26}$$

The fifth-order EHGKS takes $r = 4$ and $\hat{K} = 2$. The weights $(\omega_0, \omega_1, \omega_2) = (5/18, 4/9, 5/18)$ and $(\kappa_0, \kappa_1, \kappa_2) = (1/2 - \sqrt{15}/10, 1/2, 1/2 + \sqrt{15}/10)$ [14,26]. $\mathbb{F}^k_{i+\frac{1}{2},j}(\Delta t)$ is the second-order KFVS flux [14]. $\mathscr{G}_{i,j+\frac{1}{2}}$ can be obtained in the similar way after the local coordinate transformation.

3.2. EHGKS-SHWENO: the two-dimensional case

For convenience, we firstly define the intermediate variables: the line-average slope

$$\widehat{\mathbf{W}'^x}_{\underline{i},j_\alpha} = \frac{1}{\Delta x} \iint_{x_{i-\frac{1}{2}}}^{x_{i+\frac{1}{2}}} \frac{\partial f(x, y_{j_\alpha}, t, \mathbf{u}, \boldsymbol{\xi})}{\partial x} \boldsymbol{\Psi} \mathrm{d}\Xi \mathrm{d}x,$$

$$\widehat{\mathbf{W}'^y}_{i_\alpha,\underline{j}} = \frac{1}{\Delta y} \iint_{y_{j-\frac{1}{2}}}^{y_{j+\frac{1}{2}}} \frac{\partial f(x_{i_\alpha}, y, t, \mathbf{u}, \boldsymbol{\xi})}{\partial y} \boldsymbol{\Psi} \mathrm{d}\Xi \mathrm{d}y,$$

and the cell-average slope

$$\overline{\mathbf{W}'^x}_{i,j} = \frac{1}{\Delta x \Delta y} \iint_{I_{i,j}} \frac{\partial f(x, y, t, \mathbf{u}, \boldsymbol{\xi})}{\partial x} \boldsymbol{\Psi} \mathrm{d}\Xi \mathrm{d}x \mathrm{d}y,$$

$$\overline{\mathbf{W}'^y}_{i,j} = \frac{1}{\Delta x \Delta y} \iint_{I_{i,j}} \frac{\partial f(x, y, t, \mathbf{u}, \boldsymbol{\xi})}{\partial y} \boldsymbol{\Psi} \mathrm{d}\Xi \mathrm{d}x \mathrm{d}y.$$

They can be directly computed by

$$\widehat{\mathbf{W}'^x}_{\underline{i},j_\alpha} = \frac{1}{\Delta x} \left(\mathbf{W}(x_{i+\frac{1}{2}}, y_{j_\alpha}, t) - \mathbf{W}(x_{i-\frac{1}{2}}, y_{j_\alpha}, t) \right),$$

$$\widehat{\mathbf{W}'^y}_{i_\alpha,\underline{j}} = \frac{1}{\Delta y} \left(\mathbf{W}(x_{i_\alpha}, y_{j+\frac{1}{2}}, t) - \mathbf{W}(x_{i_\alpha}, y_{j-\frac{1}{2}}, t) \right),$$

or approximated by

$$\overline{\mathbf{W}'^x}_{i,j} \approx \sum_{\alpha=0}^{2} \widehat{\mathbf{W}'^x}_{\underline{i},j_\alpha} \omega_\alpha,$$

$$\overline{\mathbf{W}'^y}_{i,j} \approx \sum_{\alpha=0}^{2} \widehat{\mathbf{W}'^y}_{i_\alpha,\underline{j}} \omega_\alpha.$$

The evolution model of $\mathbf{W}(x_{i+\frac{1}{2}}, y_{j_\alpha}, t)$ is also available by EHGKS. According to Eqs. (23) and (7), the fifth-order evolution model of $\mathbf{W}(x_{i+\frac{1}{2}}, y_{j_\alpha}, t)$ can be evaluated by

$$\mathbf{W}(x_{i+\frac{1}{2}}, y_{j_\alpha}, t) = \left(1 - \mathrm{e}^{-\Delta t/\tau}\right) \mathbb{W}^e_{i+\frac{1}{2},j_\alpha}(t) + \mathrm{e}^{-\Delta t/\tau} \mathbb{W}^k_{i+\frac{1}{2},j_\alpha}(t), \tag{27}$$

where

$$\mathbb{W}^e_{i+\frac{1}{2},j_\alpha}(t) = \sum_{l=0}^{4} \int \frac{1}{l!} \left(t \frac{\partial}{\partial t} + y_{j_\alpha} \frac{\partial}{\partial y} \right)^l g^e \boldsymbol{\Psi} \mathrm{d}\Xi,$$

$$\mathbb{W}^k_{i+\frac{1}{2},j_\alpha}(t) = \sum_{l=0}^{1} \int \frac{(-1)^l}{l!} \left(ut \frac{\partial}{\partial x} + (vt - y_{j_\alpha}) \frac{\partial}{\partial y} \right)^l g^0 \boldsymbol{\Psi} \mathrm{d}\Xi.$$

$\mathbb{W}^e_{i+\frac{1}{2},j_\alpha}(t)$ can be approximated by

$$\mathbb{W}^e_{i+\frac{1}{2},j_\alpha}(t) \approx \mathcal{W}\left(\mathcal{Q}^e\left(y_{j_\alpha}, t\right)\right). \tag{28}$$

$\mathcal{Q}^e(y, t)$ is obtained by Eq. (26). For simple notation, we further define the intermediate variables of line averages:

$$\widehat{\mathbf{W}}_{\underline{i},j_\alpha} = \frac{1}{\Delta x} \iint_{x_{i-\frac{1}{2}}}^{x_{i+\frac{1}{2}}} f(x, y_{j_\alpha}, t, \mathbf{u}, \boldsymbol{\xi}) \boldsymbol{\Psi} \mathrm{d}\Xi \mathrm{d}x,$$

$$\widehat{\mathbf{W}}_{i_\alpha,\underline{j}} = \frac{1}{\Delta y} \iint_{y_{j-\frac{1}{2}}}^{y_{j+\frac{1}{2}}} f(x_{i_\alpha}, y, t, \mathbf{u}, \boldsymbol{\xi}) \boldsymbol{\Psi} \mathrm{d}\Xi \mathrm{d}y.$$

The two-dimensional fifth-order SHWENO reconstruction technique is implemented dimension by dimension. Based on the stencil $\{I_{\hat{i},\hat{j}}\}$ for $i-1 \le \hat{i} \le i+1$, $j-1 \le \hat{j} \le j+1$, the procedure is illustrated in the following to reconstruct $\mathbf{W}^{\mathrm{L,R}}_{i+\frac{1}{2},j_\alpha}$ and their normal and tangential derivatives $\frac{\partial^m \mathbf{W}^{\mathrm{L,R}}_{i+\frac{1}{2},j_\alpha}}{\partial x^m}$, $\frac{\partial \mathbf{W}^{\mathrm{L,R}}_{i+\frac{1}{2},j_1}}{\partial y}$ for the interface flux and variables evaluations in $\mathbf{F}(x_{i+\frac{1}{2}}, y, t)$ and $\mathbf{W}(x_{i+\frac{1}{2}}, y_{j_\alpha}, t)$.

Step (1). Conduct the one-dimensional SHWENO reconstruction along the y direction based on $\{\overline{\mathbf{W}}_{i,j-1}, \overline{\mathbf{W}'^y}_{i,j-1}, \overline{\mathbf{W}}_{i,j}, \overline{\mathbf{W}}_{i,j+1}, \overline{\mathbf{W}'^y}_{i,j+1}\}$ to obtain $\widehat{\mathbf{W}}_{\underline{i},j_\alpha}$ and $\frac{\partial \widehat{\mathbf{W}}_{\underline{i},j_1}}{\partial y}$;

Step (2). Conduct the one-dimensional SHWENO reconstruction along the x direction based on the stencil $\{\widehat{\mathbf{W}}_{\underline{i-1},j_\alpha}, \widehat{\mathbf{W}'^x}_{\underline{i-1},j_\alpha}, \widehat{\mathbf{W}}_{\underline{i},j_\alpha}, \widehat{\mathbf{W}}_{\underline{i+1},j_\alpha}, \widehat{\mathbf{W}'^x}_{\underline{i+1},j_\alpha}\}$ to obtain $\mathbf{W}^{\mathrm{L}}_{i+\frac{1}{2},j_\alpha}$, $\mathbf{W}^{\mathrm{R}}_{i-\frac{1}{2},j_\alpha}$ and their normal derivatives $\frac{\partial^m \mathbf{W}^{\mathrm{L}}_{i+\frac{1}{2},j_\alpha}}{\partial x^m}$, $\frac{\partial^m \mathbf{W}^{\mathrm{R}}_{i-\frac{1}{2},j_\alpha}}{\partial x^m}$;

Step (3). Conduct the third-order WENO reconstruction along the x direction based on $\{\frac{\partial \widehat{\mathbf{W}}_{\underline{i-1},j_1}}{\partial y}, \frac{\partial \widehat{\mathbf{W}}_{\underline{i},j_1}}{\partial y}, \frac{\partial \widehat{\mathbf{W}}_{\underline{i+1},j_1}}{\partial y}\}$ to obtain the tangential derivatives $\frac{\partial \mathbf{W}^{\mathrm{L}}_{i+\frac{1}{2},j_1}}{\partial y}$ and $\frac{\partial \mathbf{W}^{\mathrm{R}}_{i-\frac{1}{2},j_1}}{\partial y}$.

The higher-order reconstruction to obtain the tangential derivatives $\frac{\partial \mathbf{W}^{\mathrm{L}}_{i+\frac{1}{2},j_1}}{\partial y}$ and $\frac{\partial \mathbf{W}^{\mathrm{R}}_{i-\frac{1}{2},j_1}}{\partial y}$ in Step (3) is not necessary, because they exist only in the second-order KFVS flux and work near discontinuity to preserve robustness. The compactness of the stencil for the two-dimensional SHWENO reconstruction technique is preserved. In the two-dimensional case, EHGKS-SHWENO still preserves the advantages of the one-dimensional case.

By the way, to calculate the normal derivatives of $\mathbf{W}^e_{i+\frac{1}{2},j_\alpha}$, i.e., $\frac{\partial^m \mathbf{W}^e_{i+\frac{1}{2},j_\alpha}}{\partial x^m}$, the similar weighting is used as Eq. (12). In the tangential direction, the linear reconstruction is implemented based on the stencil $\{\frac{\partial^m \mathbf{W}^e_{i+\frac{1}{2},(j-1)_1}}{\partial x^m}, \frac{\partial^m \mathbf{W}^e_{i+\frac{1}{2},j_0}}{\partial x^m}, \frac{\partial^m \mathbf{W}^e_{i+\frac{1}{2},j_1}}{\partial x^m}, \frac{\partial^m \mathbf{W}^e_{i+\frac{1}{2},j_2}}{\partial x^m}, \frac{\partial^m \mathbf{W}^e_{i+\frac{1}{2},(j+1)_1}}{\partial x^m}\}$. Details can be referred in Appendix A.

Remark 2. It's possible to extend EHGKS-SHWENO to the non-uniform, and even unstructured meshes. The reconstruction in EHGKS-SHWENO contains two steps: the stencil selection and the polynomial reconstruction. In the first step, the stencil, which contains the cell-average and cell-interface variables, only need to use the target cell and its neighbor. Thus we can also find the stencil for the non-uniform meshes without introducing too much complexity. In the second step, following the ideas of the simple WENO and HWENO for the non-uniform meshes [36,10], it's possible to extend the new reconstruction of the polynomials to the non-uniform meshes. This work will be studied in the future.

4. Numerical tests

The time step Δt is determined by the CFL condition

$$\Delta t = CFL \times \min\left\{\frac{\Delta x}{|\overline{U}| + \overline{c}_s}, \frac{\Delta y}{|\overline{V}| + \overline{c}_s}\right\}, \tag{29}$$

where the speed of sound $c_s = \sqrt{\gamma RT}$. $\gamma = 1.4$. The CFL condition number is 0.8 in the one-dimensional cases and 0.4 in the two-dimensional cases if without specification.

A series of one and two-dimensional benchmark cases are tested:

(1) The one-dimensional linear advection of the density perturbation [19]: this case is to assess the accuracy and efficiency of the newly-developed scheme.

Table 1
Accuracy test for the one-dimensional advection of the density perturbation.

	EHGKS-SHWENO					
N	L_1 error	Order	L_2 error	Order	L_∞ error	Order
10	1.87E–02		2.05E–02		2.92E–02	
20	6.27E–04	4.90	6.96E–04	4.88	1.01E–03	4.85
40	1.97E–05	4.99	2.19E–05	4.99	3.20E–05	4.98
80	6.16E–07	5.00	6.84E–07	5.00	1.00E–06	5.00
160	1.93E–08	5.00	2.14E–08	5.00	3.14E–08	5.00
320	6.02E–10	5.00	6.68E–10	5.00	9.80E–10	5.00

(2) The Shu-Osher shock acoustic wave interaction [21]: this case is to test the ability of the scheme to capture the small-scale smooth features without introducing over diffusion [14].
(3) The modified shock/turbulence interaction [29]: this case is a modified test of the former one, which is more appropriate for testing the performance of very-high order schemes [29].
(4) The Woodward-Colella blast wave [24]: this test is to demonstrate the robustness of the scheme in flows with complex interactions of strong shock waves [14].
(5) The two-dimensional linear advection of the density perturbation [34]: this case is to assess the accuracy and efficiency in the two-dimensional case.
(6) The isentropic vortex propagation problem [12]: this case is to assess the accuracy and efficiency in the non-linear smooth flow.
(7) The two-dimensional Riemann problems [19,33,7]: these problems are to demonstrate the ability to solve the two-dimensional Riemann problems genuinely [14].
(8) The double Mach reflection problem [3]: this classical case is to test the ability of the scheme to capture the complex flows produced by the interactions of shock waves [14].

Comparisons on the efficiency and resolution among EHGKS-SHWENO, EHGKS-HWENO and EHGKS-WENO are also made in this section. EHGKS-SHWENO uses $\gamma_1 = 0.998, \gamma_2 = \gamma_3 = 0.001$, as a compromise between robustness and resolution. To avoid the serious robustness problem from the initial strong discontinuities, all the reconstructions are reduced to the first order if the reconstruction leads to the negative density or pressure. More strict positivity conditions will be studied in the future. Besides, the efficiency of EHGKS-SHWENO, EHGKS-WENO and the standard fifth-order Runge-Kutta scheme is compared in Appendix B.

4.1. The one-dimensional linear advection of the density perturbation

The accuracy test of EHGKS-SHWENO is carried out in this case. To demonstrate the consistent accuracy in both space and time, $CFL = 0.95$ is adopted in this case [25,28]. The comparisons on the efficiency among EHGKS-SHWENO, EHGKS-HWENO and EHGKS-WENO are also made. All the simulations are done on a single processor with Intel(R) Xeon(R) W-2102 @2.90 GHz.

The computational domain is $[0, 2\pi]$. The initial condition is

$$(\rho, U, p) = (1 + 0.2\sin x, 1, 1)\,.$$

Under the periodic boundary condition, the analytic solution is [14]

$$(\rho, U, p) = (1 + 0.2\sin(x - t), 1, 1)\,.$$

The domain is divided by N cells uniformly. The output time is 200π.

The orders of accuracy of EHGKS-SHWENO are shown in Table 1. It demonstrates EHGKS-SHWENO can achieve the designed fifth order of accuracy in both space and time.

The errors and the corresponding CPU times of EHGKS-SHWENO, EHGKS-HWENO and EHGKS-WENO are compared in Fig. 1. The CPU times in each computing time step with $N = 320$ are compared in Table 2. It demonstrates that although the CPU time per step of EHGKS-SHWENO is larger than EHGKS-HWENO and EHGKS-WENO, the efficiency of EHGKS-SHWENO is the highest, owing to the lower errors of SHWENO.

4.2. The Shu-Osher shock acoustic wave interaction

The computational domain is $[-5, 5]$. The initial flow field is [19]

$$(\rho, U, p) = \begin{cases} (3.857134, 2.629369, 10.33333)\,, & x \le -4, \\ (1 + 0.2\sin(5x), 0, 1)\,, & x > -4. \end{cases}$$

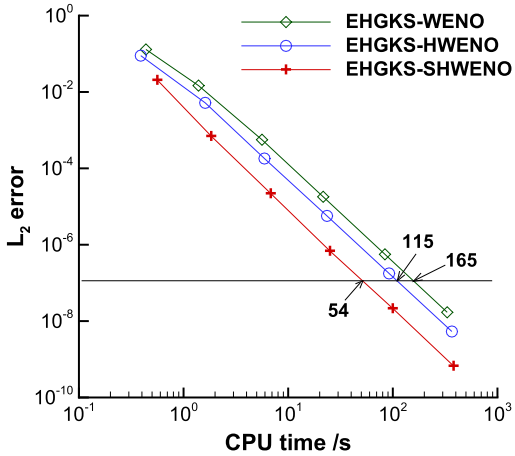

Fig. 1. The CPU time vs L_2 error. The test case is the one-dimensional advection of the density perturbation.

Table 2
The CPU time (seconds) per time step in the one-dimensional advection of the density perturbation with 320 cells.

	CPU time per step
EHGKS-SHWENO	4.87E–03
EHGKS-HWENO	4.69E–03
EHGKS-WENO	4.23E–03

The domain is divided by 200 and 400 cells uniformly. The output time $t = 1.8$. The reference solution is calculated from the refined grids.

The density profiles and the local enlargement of EHGKS-SHWENO, EHGKS-HWENO and EHGKS-WENO are shown in Fig. 2. Comparisons show the resolution of both the compact EHGKS-HWENO and EHGKS-SHWENO is better than that of EHGKS-WENO. And the acoustic oscillations are better captured by EHGKS-SHWENO than EHGKS-HWENO.

4.3. The modified shock/turbulence interaction

The computational domain is $[-5, 5]$. The initial flow field is [29]

$$(\rho, U, p) = \begin{cases} (1.515695, 0.523346, 1.80500), & x \le -4.5, \\ (1 + 0.1\sin(20\pi x), 0, 1), & x > -4.5. \end{cases}$$

The domain is divided by 1000 cells uniformly. The output time $t = 5$. The reference solution is calculated from 5000 uniform cells by EHGKS-SHWENO.

The local enlargement of the density profiles of EHGKS-SHWENO, EHGKS-HWENO and EHGKS-WENO are shown in Fig. 3. Comparisons again show the best resolution of EHGKS-SHWENO among the three schemes.

4.4. The Woodward-Colella blast wave

The computational domain is $[0, 1]$. The initial flow field is [7]

$$(\rho, U, p) = \begin{cases} (1, 0, 1000), & 0 \le x \le 0.1, \\ (1, 0, 0.01), & 0.1 < x \le 0.9, \\ (1, 0, 100), & 0.9 < x \le 1. \end{cases}$$

The reflective boundary condition is adopted on both sides of the domain. The domain is divided by 400 cells uniformly. The output time $t = 0.038$.

Comparisons in Fig. 4 draw the same conclusion in the previous case that the density distributions are better captured by EHGKS-SHWENO than EHGKS-HWENO and EHGKS-WENO, especially at the discontinuity and the local extreme.

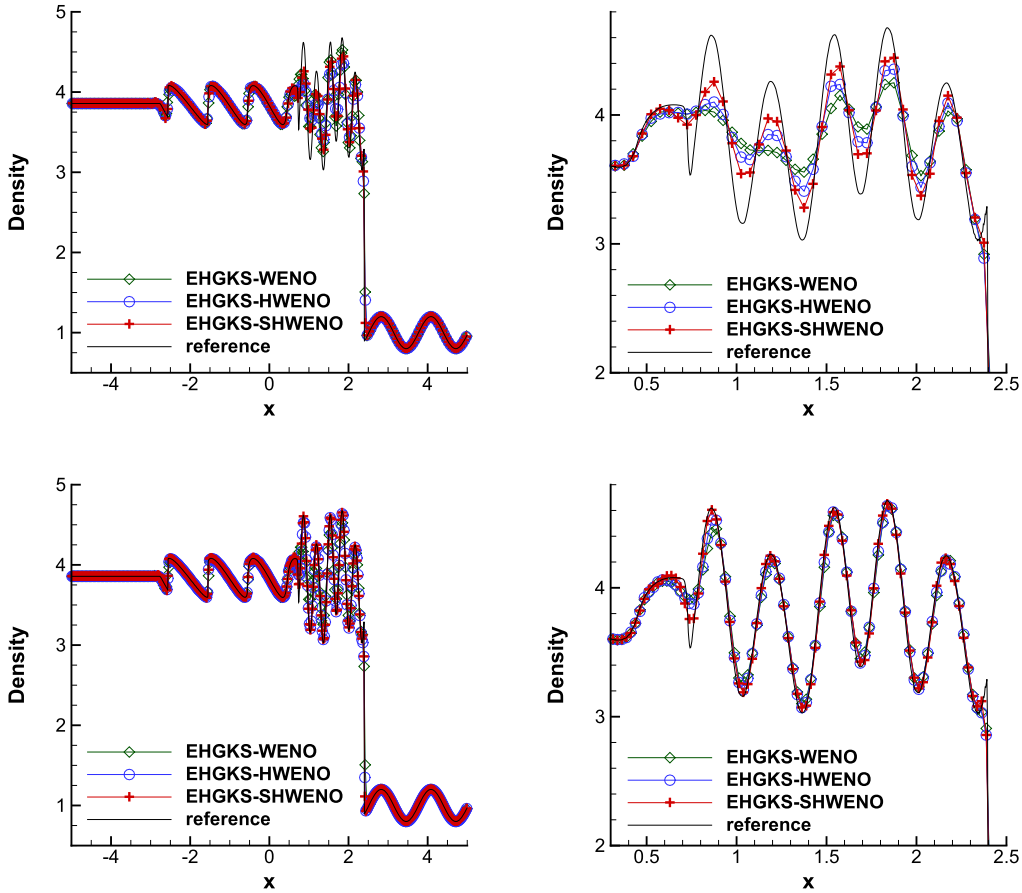

Fig. 2. The density profile of the Shu-Osher shock acoustic wave interaction with 200 (top) and 400 (bottom) uniform cells at $t = 1.8$.

Table 3
Accuracy test for the two-dimensional advection of the density perturbation.

	EHGKS-SHWENO					
N	L_1 error	Order	L_2 error	Order	L_∞ error	Order
20	8.48E–06		1.09E–05		3.22E–05	
40	1.16E–07	6.20	1.35E–07	6.34	3.55E–07	6.50
80	3.54E–09	5.03	3.92E–09	5.11	6.13E–09	5.86
160	1.10E–10	5.01	1.21E–10	5.01	1.77E–10	5.12

4.5. The two-dimensional linear advection of the density perturbation

In this case, the initial flow field is

$$(\rho, U, V, p) = (1 + 0.2\sin(x + y), 0.7, 0.3, 1)\,.$$

The computational domain is $[0, 2\pi] \times [0, 2\pi]$. Under the periodic boundary condition, the analytic solution is [14]

$$(\rho, U, V, p) = (1 + 0.2\sin(x + y - t), 0.7, 0.3, 1)\,.$$

The domain is divided by $N \times N$ cells uniformly. $CFL = 0.45$ is adopted in this case. The output time $t = 2\pi$.

The orders of accuracy of EHGKS-SHWENO are shown in Table 3, illustrating the designed fifth order of accuracy is achieved.

The efficiency of EHGKS-SHWENO, EHGKS-HWENO and EHGKS-WENO is compared in Fig. 5. The higher efficiency of EHGKS-SHWENO over EHGKS-HWENO and EHGKS-WENO is also validated.

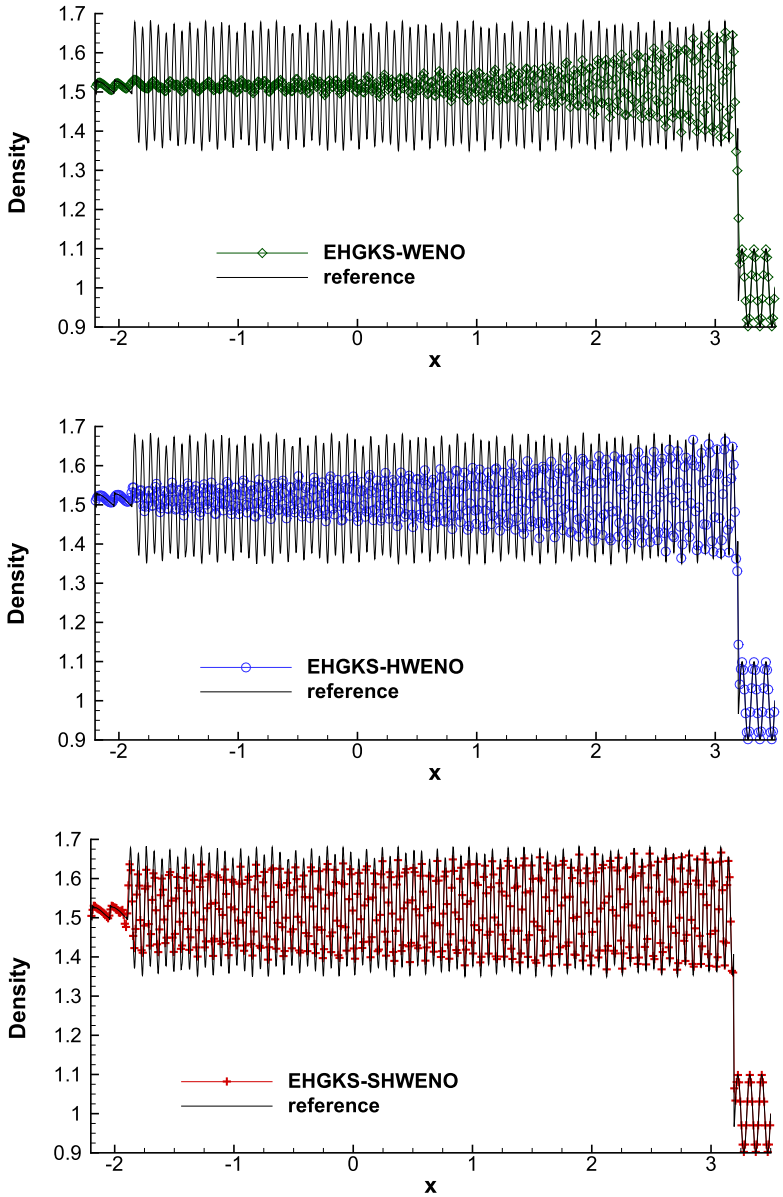

Fig. 3. The density profile of the modified shock/turbulence interaction with 1000 uniform cells at $t = 5$.

4.6. The isentropic vortex propagation problem

The computational domain is $[-0.5, 0.5] \times [-0.5, 0.5]$. The initial flow field is a mean flow

$$(\rho, U, V, p) = (1, 1, 1, 1),$$

with an isentropic vortex, i.e., no perturbation in entropy $S = p/\rho^{\gamma}$. The perturbations in velocities and temperature are

$$(\delta U, \delta V) = \frac{10\varepsilon}{2\pi} e^{\frac{1-\eta^2}{2}} (-y, x), \delta T = -\frac{(\gamma - 1)\varepsilon^2}{8\gamma\pi^2} e^{1-\eta^2},$$

where $\varepsilon = 5$ and $\eta^2 = 100(x^2 + y^2)$ [14]. Under the periodic boundary condition, the analytic solution is the vortex along the upper right direction with velocities $(U, V) = (1, 1)$. The domain is divided by $N \times N$ cells uniformly. $CFL = 0.45$ is adopted in this case. The output time $t = 1$.

The orders of accuracy based on the density are shown in Table 4. It validates EHGKS-SHWENO can achieve the designed fifth order of accuracy in this non-linear smooth flow.

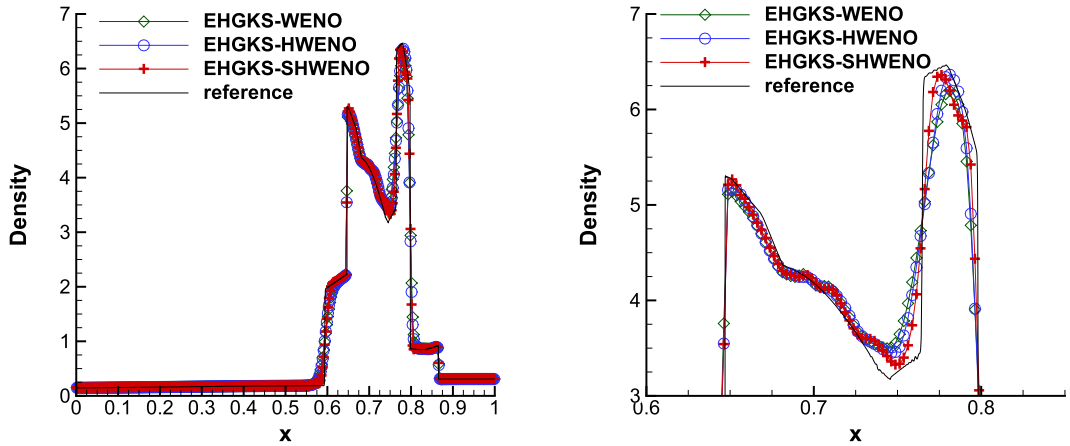

Fig. 4. The density profile of the Woodward-Colella blast wave problem with 400 uniform cells at $t = 0.038$.

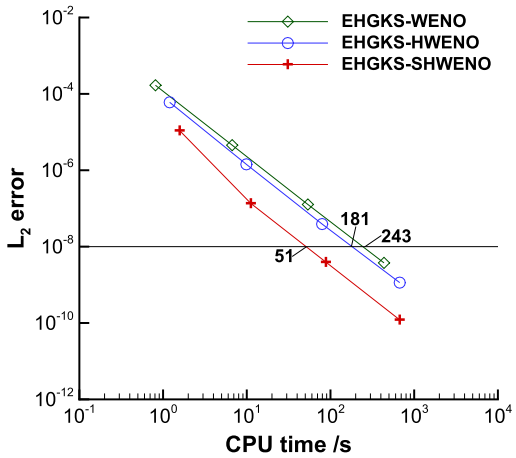

Fig. 5. The CPU time vs L_2 error. The test case is the two-dimensional advection of the density perturbation.

Table 4
Accuracy test for the two-dimensional isentropic vortex propagation.

	EHGKS-SHWENO					
N	L_1 error	Order	L_2 error	Order	L_∞ error	Order
80	5.58E−06		1.87E−05		2.63E−04	
160	1.06E−07	5.72	2.88E−07	6.02	2.74E−06	6.58
320	3.55E−09	4.90	8.85E−09	5.03	5.90E−08	5.54

The efficiency of EHGKS-SHWENO, EHGKS-HWENO and EHGKS-WENO is compared in Fig. 6. It also shows the efficiency of EHGKS-SHWENO is higher than EHGKS-HWENO and EHGKS-WENO.

4.7. The two-dimensional Riemann problems

The first case is the interaction between shocks and contact continuities [7,19]. The computational domain is $[0, 1] \times [0, 1]$. The initial flow field is

$$(\rho, U, V, p) = \begin{cases} (1.5, 0, 0, 1.5), & x \geq 0.7, y \geq 0.7, \\ (0.5323, 1.206, 0, 0.3), & x < 0.7, y \geq 0.7, \\ (0.138, 1.206, 1.206, 0.029), & x < 0.7, y < 0.7, \\ (0.5323, 0, 1.206, 0.3), & x \geq 0.7, y < 0.7. \end{cases}$$

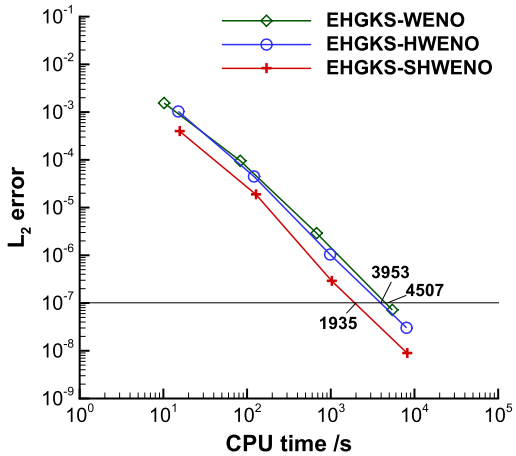

Fig. 6. The CPU time vs L_2 error. The test case is the two-dimensional isentropic vortex propagation.

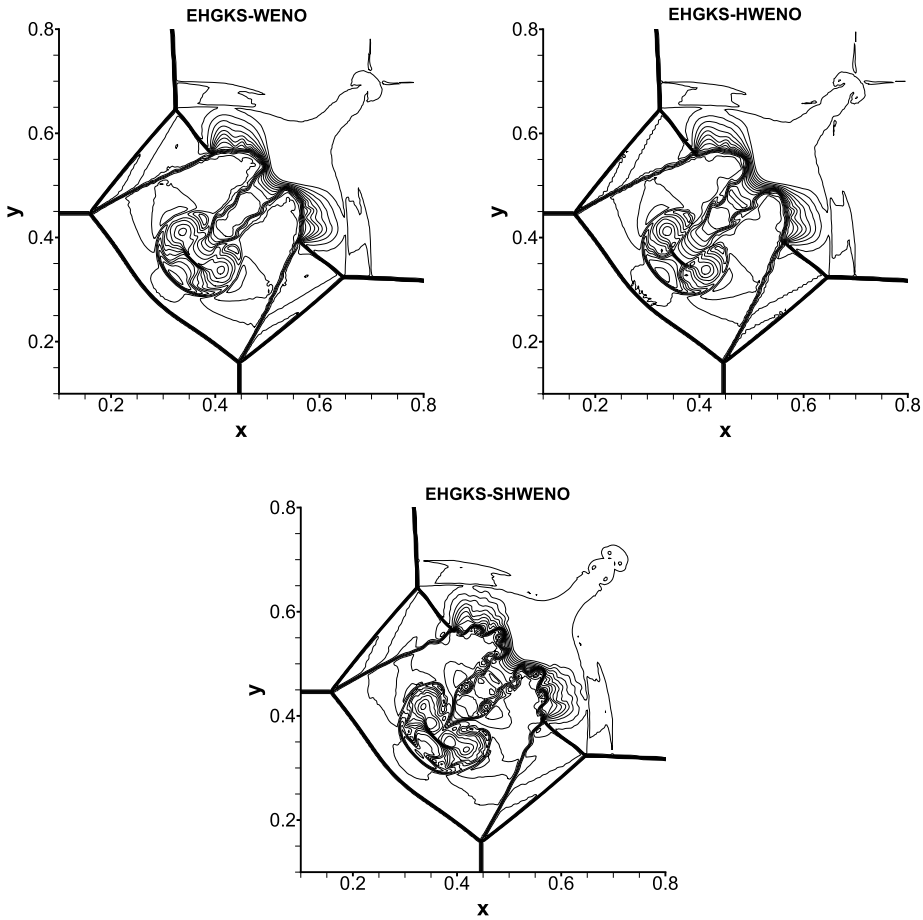

Fig. 7. The density distribution of the first two-dimensional Riemann problem at $t = 0.6$ with 400×400 uniform cells. 23 contours are drawn from 0.15 to 1.5.

The non-reflecting boundary condition is used at all boundaries. The output time is 0.6. The domain is divided by 400×400 cells uniformly. The density distributions from EHGKS-SHWENO, EHGKS-HWENO and EHGKS-WENO are shown in Fig. 7. The results show the interactions between the shocks and the contact continuities are better captured by EHGKS-SHWENO than the others.

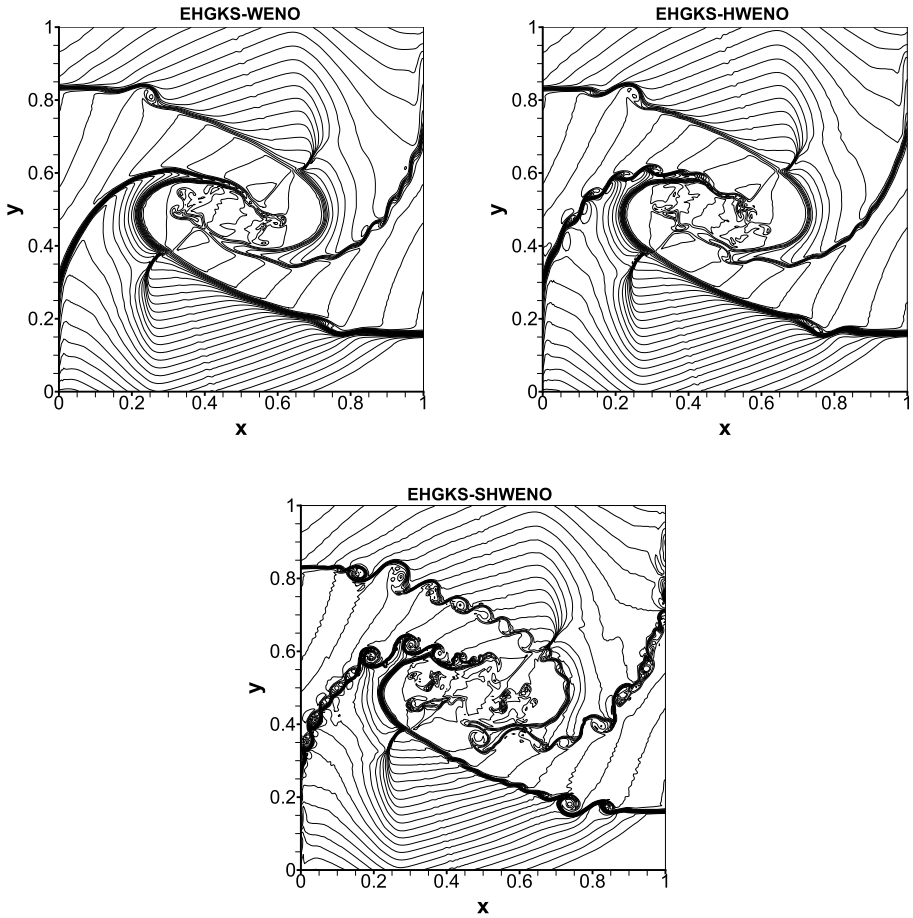

Fig. 8. The density distribution of the second two-dimensional Riemann problem at $t = 0.8$ with 300×300 uniform cells. 30 contours are drawn from 0.2 to 2.2.

The second problem is the shear instabilities among four initial contact discontinuities [8,7,33]. The computational domain is $[0, 1] \times [0, 1]$. The initial flow field is

$$(\rho, U, V, p) = \begin{cases} (1, 0.75, -0.5, 1), & x \geq 0.5, y \geq 0.5, \\ (2, 0.75, 0.5, 1), & x < 0.5, y \geq 0.5, \\ (1, -0.75, 0.5, 1), & x < 0.5, y < 0.5, \\ (3, -0.75, -0.5, 1), & x \geq 0.5, y < 0.5. \end{cases}$$

The non-reflecting boundary condition is used at all boundaries. The output time is 0.8. The domain is divided by 300×300 cells uniformly. The density distributions in Fig. 8 show the roll-up is better captured by EHGKS-SHWENO than EHGKS-HWENO and EHGKS-WENO.

4.8. The double Mach reflection problem

In this case, a right-moving shock of $\mathrm{Ma} = 10$ is initially positioned at $(x, y) = (\frac{1}{6}, 0)$ with $60°$ to the wall [31]. The pre-shock condition is

$$(\rho, U, V, p) = \left(8, 4.125\sqrt{3}, -4.125, 116.5\right),$$

and the post-shock condition is

$$(\rho, U, V, p) = (1.4, 0, 0, 1).$$

The computational domain is $[0, 3] \times [0, 0.75]$, divided by 720×180 and 1440×360 cells uniformly. The pre-shock and post-shock conditions are imposed at the left, right, top and bottom boundaries to describe the exact motion of the shock, except that the reflective boundary condition is implemented at the wall [14]. The output time is 0.2.

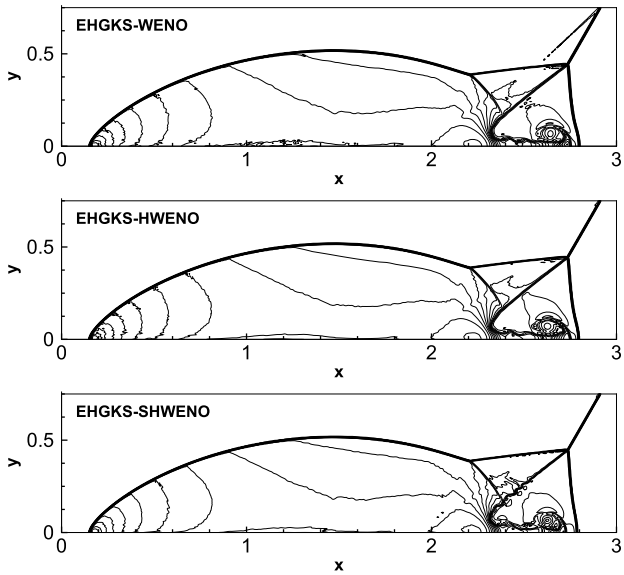

Fig. 9. The density distribution of the double Mach reflection problem at $t = 0.2$ with $\Delta x = \Delta y = 1/240$. 30 contours are drawn from 1.731 to 20.92.

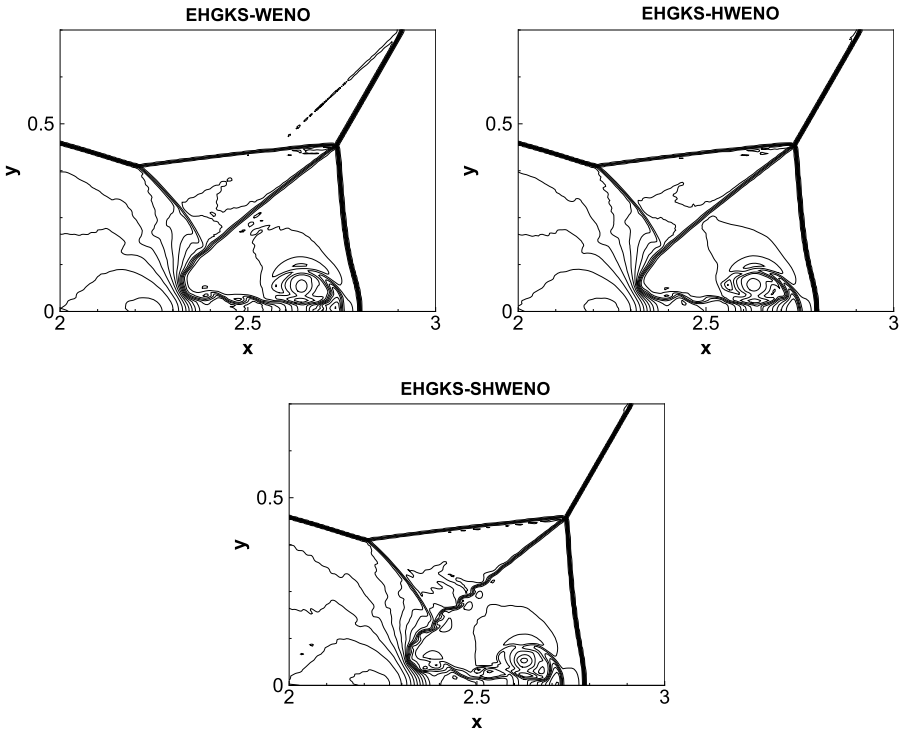

Fig. 10. The enlarged density distribution of the double Mach reflection problem at $t = 0.2$ with $\Delta x = \Delta y = 1/240$. 30 contours are drawn from 1.731 to 20.92.

The comparisons on the density distributions are shown in Figs. 9 to 12. The results of EHGKS-SHWENO show better resolution on the instabilities of the contact line from the triple Mach stem than EHGKS-HWENO and EHGKS-WENO.

5. Conclusions

Based on the framework of EHGKS and the newly-developed SHWENO reconstruction technique, a compact one-stage scheme is proposed to solve the Euler equations of compressible flows with fifth-order accuracy in both space and time. EHGKS provides both the time-dependent flux and variables at cell interfaces, making it possible to compute directly the

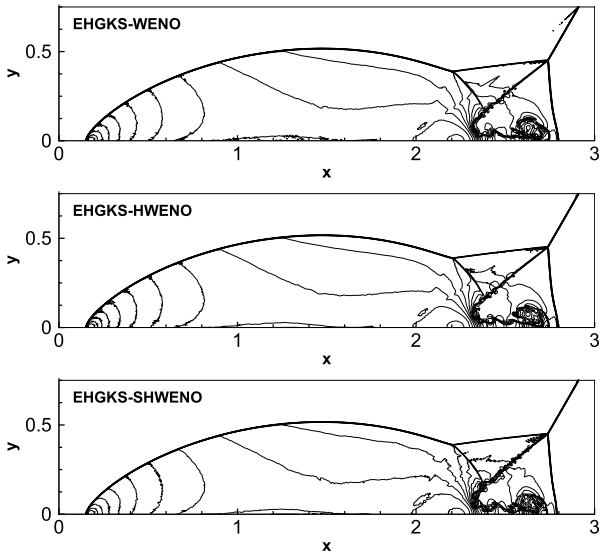

Fig. 11. The density distribution of the double Mach reflection problem at $t = 0.2$ with $\Delta x = \Delta y = 1/480$. 30 contours are drawn from 1.731 to 20.92.

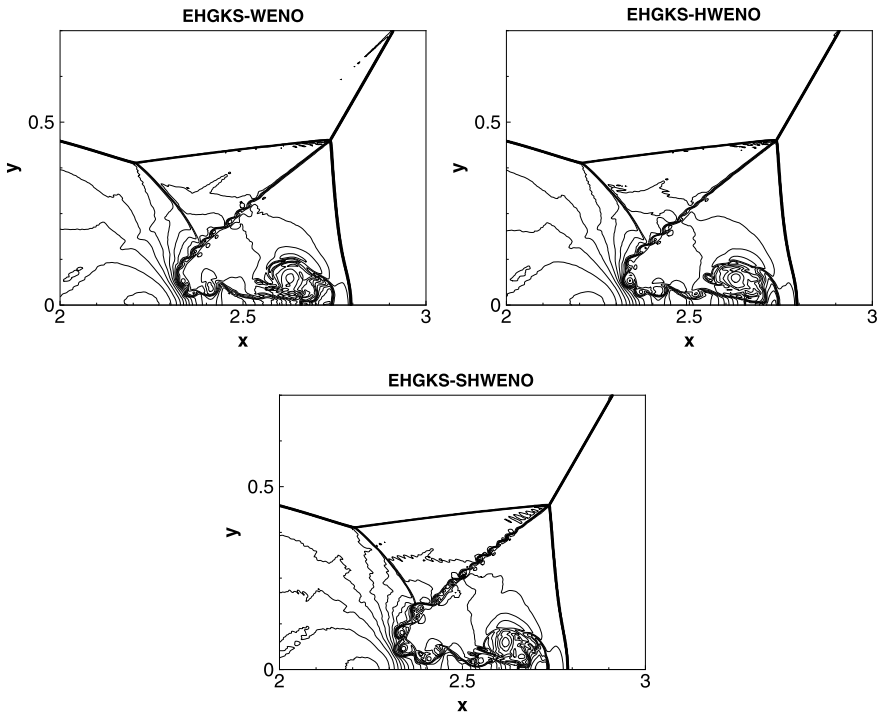

Fig. 12. The enlarged density distribution of the double Mach reflection problem at $t = 0.2$ with $\Delta x = \Delta y = 1/480$. 30 contours are drawn from 1.731 to 20.92.

cell-average slope values, instead of solving additional equations for the slope. SHWENO takes both the advantage of simple WENO to reconstruct the polynomial over the cell and HWENO for a compact stencil. Different from the current compact multi-stage schemes, EHGKS-SHWENO evolves and reconstructs only once in each computing time step.

Several benchmark tests are carried out to demonstrate the accuracy and efficiency of the new scheme. In these cases, EHGKS-SHWENO gives good resolution on the shock discontinuities and flow details. Comparisons among EHGKS-SHWENO, EHGKS-HWENO and EHGKS-WENO validate the high efficiency of the new scheme.

CRediT authorship contribution statement

Shiyi Li: Conceptualization, Data curation, Methodology, Software, Writing – original draft, Writing – review & editing. **Dongmi Luo:** Methodology, Software, Writing – original draft, Writing – review & editing. **Jianxian Qiu:** Conceptualization,

Supervision, Writing – original draft, Writing – review & editing. **Yibing Chen:** Conceptualization, Methodology, Project administration, Writing – original draft, Writing – review & editing.

Declaration of competing interest

The authors declare that they have no known competing financial interests or personal relationships that could have appeared to influence the work reported in this paper.

Acknowledgements

This work is supported by NSFC (Grant Nos. 11901044, 12101063, 12071392), the Science Challenge Project (Grant No. TZ2016002) and the National Key Project (Grant No. GJXM92579).

Appendix A. The reconstruction of the tangential derivatives of $\mathbf{W}^e_{i+\frac{1}{2},j_1}$

Conduct the linear reconstruction along the y direction based on the stencil $\{\frac{\partial^m \mathbf{W}^e_{i+\frac{1}{2},(j-1)_1}}{\partial x^m}, \frac{\partial^m \mathbf{W}^e_{i+\frac{1}{2},j_0}}{\partial x^m}, \frac{\partial^m \mathbf{W}^e_{i+\frac{1}{2},j_1}}{\partial x^m}, \frac{\partial^m \mathbf{W}^e_{i+\frac{1}{2},j_2}}{\partial x^m}, \frac{\partial^m \mathbf{W}^e_{i+\frac{1}{2},(j+1)_1}}{\partial x^m}\}$. The tangential derivatives of $\mathbf{W}^e_{i+\frac{1}{2},j_1}$, i.e. $\frac{\partial^{m+l}}{\partial x^m y^l}\mathbf{W}^e_{i+\frac{1}{2},j_1}$ for $1 \le l \le 4$ are

$$
\begin{aligned}
\frac{\partial^{m+1}\mathbf{W}^e_{i+\frac{1}{2},j_1}}{\partial x^m y} &= \frac{3}{34\Delta y}\frac{\partial^m \mathbf{W}^e_{i+\frac{1}{2},(j-1)_1}}{\partial x^m} - \frac{20\sqrt{15}}{51\Delta y}\frac{\partial^m \mathbf{W}^e_{i+\frac{1}{2},j_0}}{\partial x^m} \\
&\quad - \frac{3}{34\Delta y}\frac{\partial^m \mathbf{W}^e_{i+\frac{1}{2},(j+1)_1}}{\partial x^m} + \frac{20\sqrt{15}}{51\Delta y}\frac{\partial^m \mathbf{W}^e_{i+\frac{1}{2},j_2}}{\partial x^m}, \\
\frac{\partial^{m+2}\mathbf{W}^e_{i+\frac{1}{2},j_1}}{\partial x^m y^2} &= -\frac{3}{17\Delta y^2}\frac{\partial^m \mathbf{W}^e_{i+\frac{1}{2},(j-1)_1}}{\partial x^m} + \frac{400}{51\Delta y^2}\frac{\partial^m \mathbf{W}^e_{i+\frac{1}{2},j_0}}{\partial x^m} \\
&\quad - \frac{3}{17\Delta y^2}\frac{\partial^m \mathbf{W}^e_{i+\frac{1}{2},(j+1)_1}}{\partial x^m} + \frac{400}{51\Delta y^2}\frac{\partial^m \mathbf{W}^e_{i+\frac{1}{2},j_2}}{\partial x^m} - \frac{46}{3\Delta y^2}\frac{\partial^m \mathbf{W}^e_{i+\frac{1}{2},j_1}}{\partial x^m}, \\
\frac{\partial^{m+3}\mathbf{W}^e_{i+\frac{1}{2},j_1}}{\partial x^m y^3} &= -\frac{60}{17\Delta y^3}\frac{\partial^m \mathbf{W}^e_{i+\frac{1}{2},(j-1)_1}}{\partial x^m} + \frac{40\sqrt{15}}{17\Delta y^3}\frac{\partial^m \mathbf{W}^e_{i+\frac{1}{2},j_0}}{\partial x^m} \\
&\quad + \frac{60}{17\Delta y^3}\frac{\partial^m \mathbf{W}^e_{i+\frac{1}{2},(j+1)_1}}{\partial x^m} - \frac{40\sqrt{15}}{17\Delta y^3}\frac{\partial^m \mathbf{W}^e_{i+\frac{1}{2},j_2}}{\partial x^m}, \\
\frac{\partial^{m+4}\mathbf{W}^e_{i+\frac{1}{2},j_1}}{\partial x^m y^4} &= \frac{240}{17\Delta y^4}\frac{\partial^m \mathbf{W}^e_{i+\frac{1}{2},(j-1)_1}}{\partial x^m} - \frac{1600}{17\Delta y^4}\frac{\partial^m \mathbf{W}^e_{i+\frac{1}{2},j_0}}{\partial x^m} \\
&\quad + \frac{240}{17\Delta y^4}\frac{\partial^m \mathbf{W}^e_{i+\frac{1}{2},(j+1)_1}}{\partial x^m} - \frac{1600}{17\Delta y^4}\frac{\partial^m \mathbf{W}^e_{i+\frac{1}{2},j_2}}{\partial x^m} + \frac{160}{\Delta y^4}\frac{\partial^m \mathbf{W}^e_{i+\frac{1}{2},j_1}}{\partial x^m}.
\end{aligned}
$$

Appendix B. Comparisons between EHGKS and the fifth-order Runge-Kutta scheme

The comparisons of the one-stage EHGKS and the multi-stage Runge-Kutta method are made in this section. For better illustration on their different performance by the temporal discretization, the standard fifth-order six-stage Runge-Kutta method [9,6] is performed with the GKS flux (only the first-order GKS is required in the Runge-Kutta method [9,14]) and the WENO reconstruction. It is denoted by RK5-WENO.

Table B.5
The CPU time (seconds) per time step in the one-dimensional advection of the density perturbation with $N = 320$ cells.

	CPU time per step
EHGKS-SHWENO	4.87E–03
EHGKS-WENO	4.23E–03
RK5-WENO	7.33E–03

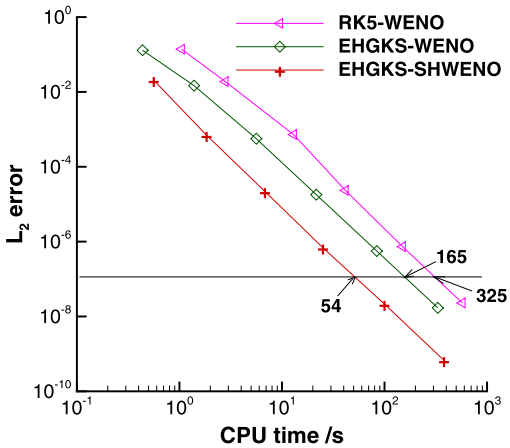

Fig. B.13. The CPU time vs L_2 error. The test case is the one-dimensional advection of the density perturbation.

The one-dimensional linear advection of the density perturbation is tested. The computational parameters can be referred in Section 4.1.

The CPU times per time step are present in Table B.5. It illustrates that the CPU time per step of RK5-WENO is larger than both EHGKS-WENO and EHGKS-SHWENO. As shown in Fig. B.13, the efficiency of EHGKS-WENO and EHGKS-SHWENO is higher than RK5-WENO.

References

[1] R. Abgrall, Residual distribution schemes: current status and future trends, Comput. Fluids 35 (7) (2006) 641–669.
[2] M. Castro, B. Costa, W.S. Don, High order weighted essentially non-oscillatory WENO-Z schemes for hyperbolic conservation laws, J. Comput. Phys. 230 (5) (2011) 1766–1792.
[3] Y.B. Chen, S. Jiang, N. Liu, HFVS: an arbitrary high order approach based on flux vector splitting, J. Comput. Phys. 322 (2016) 708–722.
[4] B. Cockburn, C.W. Shu, The Runge-Kutta discontinuous Galerkin method for conservation laws V: multidimensional systems, J. Comput. Phys. 141 (2) (1998) 199–224.
[5] Z.F. Du, J.Q. Li, A Hermite WENO reconstruction for fourth order temporal accurate schemes based on the GRP solver for hyperbolic conservation laws, J. Comput. Phys. 355 (2018) 385–396.
[6] E. Fehlberg, Low-order classical Runge–Kutta formulas with stepsize control and their application to some heat transfer problems, NASA Technical Report NASA-TR-R-315, 1969, pp. 1–43.
[7] X. Ji, L. Pan, W. Shyy, K. Xu, A compact fourth-order gas-kinetic scheme for the Euler and Navier–Stokes equations, J. Comput. Phys. 372 (2018) 446–472.
[8] X. Ji, K. Xu, Performance enhancement for high-order gas-kinetic scheme based on WENO-adaptive-order reconstruction, Commun. Comput. Phys. (2020) 539–590.
[9] X. Ji, F.X. Zhao, W. Shyy, K. Xu, A family of high-order gas-kinetic schemes and its comparison with Riemann solver based high-order methods, J. Comput. Phys. 356 (2018) 150–173.
[10] X. Ji, F.X. Zhao, W. Shyy, K. Xu, A HWENO reconstruction based high-order compact gas-kinetic scheme on unstructured mesh, J. Comput. Phys. 410 (2020) 109367.
[11] G.S. Jiang, C.W. Shu, Efficient implementation of weighted ENO schemes, J. Comput. Phys. 126 (1) (1996) 202–228.
[12] J.Q. Li, Z.F. Du, A two-stage fourth order time-accurate discretization for Lax–Wendroff type flow solvers I: hyperbolic conservation laws, SIAM J. Sci. Comput. 38 (5) (2016) A3046–A3069.
[13] Q.B. Li, K. Xu, S. Fu, A high-order gas-kinetic Navier-Stokes flow solver, J. Comput. Phys. 229 (19) (2010) 6715–6731.
[14] S.Y. Li, Y.B. Chen, S. Jiang, An efficient high-order gas-kinetic scheme (I): Euler equations, J. Comput. Phys. 415 (2020) 109488.
[15] N. Liu, H.Z. Tang, A high-order accurate gas-kinetic scheme for one and two-dimensional flow simulation, Commun. Comput. Phys. 15 (4) (2014) 911–943.
[16] J. Luo, K. Xu, A high-order multidimensional gas-kinetic scheme for hydrodynamic equations, Sci. China, Technol. Sci. 56 (10) (2013) 2370–2384.
[17] M.R. Norman, Hermite WENO limiting for multi-moment finite-volume methods using the ADER-DT time discretization for 1-D systems of conservation laws, J. Comput. Phys. 282 (2015) 381–396.
[18] L. Pan, K. Xu, High-order gas-kinetic scheme with three-dimensional WENO reconstruction for the Euler and Navier-Stokes solutions, Comput. Fluids 198 (2020) 104401.
[19] L. Pan, K. Xu, Q.B. Li, J.Q. Li, An efficient and accurate two-stage fourth-order gas-kinetic scheme for the Euler and Navier-Stokes equations, J. Comput. Phys. 326 (2016) 197–221.
[20] J.X. Qiu, Hermite WENO schemes with Lax-Wendroff type time discretizations for Hamilton-Jacobi equations, J. Comput. Math. 2 (2007) 131–144.
[21] J.X. Qiu, C.W. Shu, Hermite WENO schemes and their application as limiters for Runge-Kutta discontinuous Galerkin method: one-dimensional case, J. Comput. Phys. 193 (1) (2004) 115–135.
[22] J.X. Qiu, C.W. Shu, Hermite WENO schemes and their application as limiters for Runge-Kutta discontinuous Galerkin method II: two dimensional case, Comput. Fluids 34 (6) (2005) 642–663.
[23] C. Shen, Rarefied Gas Dynamics: Fundamentals, Simulations and Micro Flows, Springer Science & Business Media, 2006.
[24] C.W. Shu, Essentially non-oscillatory and weighted essentially non-oscillatory schemes for hyperbolic conservation laws, in: Advanced Numerical Approximation of Nonlinear Hyperbolic Equations, Springer, 1998, pp. 325–432.
[25] V.A. Titarev, E.F. Toro, ADER: arbitrary high order Godunov approach, J. Sci. Comput. 17 (1–4) (2002) 609–618.
[26] V.A. Titarev, E.F. Toro, Finite-volume WENO schemes for three-dimensional conservation laws, J. Comput. Phys. 201 (2004) 238–260.

[27] E.F. Toro, Riemann Solvers and Numerical Methods for Fluid Dynamics: A Practical Introduction, Springer Science & Business Media, 2013.
[28] E.F. Toro, R.C. Millington, L. Nejad, Towards very high order Godunov schemes, in: Godunov Methods, Springer, 2001, pp. 907–940.
[29] E.F. Toro, V.A. Titarev, TVD fluxes for the high-order ADER schemes, J. Sci. Comput. 24 (3) (2005) 285–309.
[30] Z.J. Wang, Spectral (finite) volume method for conservation laws on unstructured grids: basic formulation, J. Comput. Phys. 178 (1) (2002) 210–251.
[31] P. Woodward, P. Colella, The numerical simulation of two-dimensional fluid flow with strong shocks, J. Comput. Phys. 54 (1) (1984) 115–173.
[32] K. Xu, A gas-kinetic BGK scheme for the Navier-Stokes equations and its connection with artificial dissipation and Godunov method, J. Comput. Phys. 171 (1) (2001) 289–335.
[33] F.X. Zhao, L. Pan, Z. Li, S.H. Wang, A new class of high-order weighted essentially non-oscillatory schemes for hyperbolic conservation laws, Comput. Fluids 159 (2017) 81–94.
[34] X.H. Zhong, C.W. Shu, A simple weighted essentially nonoscillatory limiter for Runge-Kutta discontinuous Galerkin methods, J. Comput. Phys. 232 (1) (2013) 397–415.
[35] J. Zhu, J.X. Qiu, A new type of finite volume WENO schemes for hyperbolic conservation laws, J. Sci. Comput. 73 (2) (2017) 1338–1359.
[36] J. Zhu, J.X. Qiu, New finite volume weighted essentially nonoscillatory schemes on triangular meshes, J. Sci. Comput. 40 (2) (2018) 903–928.